Silicon Photonic Microring Resonators: Design Optimization Under Fabrication Non-Uniformity

Asif Mirza, Febin Sunny, Sudeep Pasricha, and Mahdi Nikdast

Department of Electrical and Computer Engineering, Colorado State University, Fort Collins, Colorado, USA {asifmirz, psfebin, sudeep, mnikdast}@colostate.edu

Abstract—Microring resonators (MRRs) are very often considered as the primary building block in silicon photonic integrated circuits (PICs). Despite many advantages, MRRs are considerably sensitive to fabrication non-uniformity (a.k.a. fabrication process variations), necessitating the use of power-hungry compensation methods (e.g., thermal tuning) to guarantee their reliable operation. Moreover, the design space of MRRs is complicated and includes several highly correlated design parameters, preventing designers from easily exploring and optimizing the design of MRRs against fabrication process variations (FPVs). In this paper, for the first time, we present a comprehensive design space exploration and optimization of MRRs against FPVs. In particular, we indicate how physical design parameters in MRRs can be optimized during design time to enhance their tolerance to FPVs while also improving the insertion loss and quality factor in such devices. Fabrication results obtained by measuring multiple fabricated MRRs designed using our design optimization solution demonstrate a significant 70% improvement on average in MRRs tolerance to different FPVs. Such improvement indicates the efficiency of our novel design optimization solution in reducing the tuning power required for reliable operation of MRRs.

Index Terms—Fabrication process variations, silicon photonics, mciroring resonators, design for reliability, design optimization.

I. Introduction

Silicon photonics (SiPh) offers new and unique solutions where today's conventional technologies are approaching their limits in terms of speed, capacity, and accuracy. Silicon photonic integrated circuits (PICs) are emerging to boost the communication performance in high-performance computing systems [1], data centers [2], and are rapidly evolving into other applications, such as neural networks [3]. Among various SiPh devices designed for PICs, microring resonators (MRRs, an example of which is shown in Fig.1(a)) are widely considered as the primary building block in such circuits in many applications because of their compact footprint (*e.g.*, radius of 3 μ m [4]) and capability to perform a variety of functions. Optical filtering, modulation, and spatial switching are some examples of the key applications of MRRs [5].

An MRR is on resonance when an optical wavelength on its input matches with the resonant wavelength of the MRR (see Figs. 1(a) and 1(b)). This resonant wavelength is jointly determined by several key parameters in the MRR design space, including the radius and the waveguide physical dimensions (*i.e.*, width and thickness), as shown in Figs. 1(a) and 1(c). Reliable operation in PICs that integrate thousands of

This research was supported by the National Science Foundation (NSF) under grant number CCF-1813370.

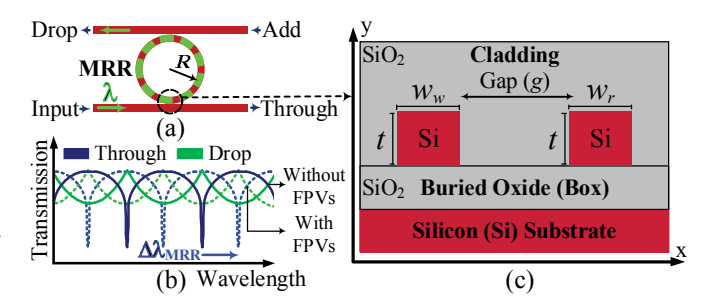


Fig. 1. (a) A passive MRR-based add-drop filter on resonance in which the input wavelength λ is coupled and dropped into the MRR (R is radius); (b) The impact of FPVs on the resonant wavelength in MRRs: optical spectrum of an MRR without FPVs (solid lines) and with FPVs (dotted lines) under which the resonant wavelength is shifted by $\Delta\lambda_{MRR}$; and, (c) Cross-section of the coupling region (circled in (a)) in an MRR in which w_w is the input or drop waveguide width, w_r is the MRR waveguide width, and t is the SOI or waveguide thickness. Unlike t that is wafer dependent, both w_w and w_r can be determined during design time.

MRRs depends on precise matching of central wavelengths of MRRs in such circuits [6]. However, MRRs are considerably sensitive to fabrication process variations (FPVs) that deviate the resonant wavelength of MRRs ($\Delta\lambda_{MRR}$ in Fig. 1(b)), resulting in severe performance and reliability degradation in PICs [7]. FPVs stem from optical lithography imperfections in which silicon-on-insulator (SOI) thickness and waveguide width variations are the major concerns [6], [8]. Consequently, PICs require efficient methods to compensate for the impact of such inevitable FPVs.

Several methods have been proposed to compensate for the impact of FPVs in PICs integrating MRRs, including the use of high energy particles as well as thermal tuning [9]. Nevertheless, these methods are power-hungry and lead to considerable increase in power dissipation in PICs. For example, using an internal integrated heater, one can adjust the resonant wavelength of an MRR by 1.2 nm/mW [10]. This rather small power consumption will quickly add up in PICs integrating a large number of MRRs, where each MRR resonant wavelength may need to be adjusted by ≈9 nm as indicated in previous experimental studies [8]. Recently, some efforts have been made to study the design space of MRRs with a goal of increasing their tolerance to FPVs [11]-[13], and hence minimizing the required tuning in such devices. These works, however, failed to present any details on how to find optimal design parameters in MRRs under FPVs, and ignored the impact of their proposed solutions on insertion loss and quality factor (Q-factor) in MRRs. Indeed, altering MRR design parameters (e.g., increasing the waveguide width proposed in [11], [12]) affects the insertion loss and Q-factor in these devices, which are two fundamental performance metrics when designing MRRs.

The novel contribution of this paper is in a comprehensive design space exploration of MRRs to optimize their performance against different FPVs. In particular, we present a novel design optimization solution that not only enhances tolerance in MRRs to FPVs, but also improves their insertion loss and Q-factor. We consider passive MRRs that are widely used for wavelength-selective switching and optical filtering in PICs. We first explore and model the impact of different FPVs (i.e., those in SOI thickness and waveguide width) on the resonant wavelength of MRRs, identifying the impact of each variation on the resonant wavelength shift in MRRs. Also, we present models for the coupling, which impacts the insertion loss, and Q-factor in MRRs, all of which include the impact of FPVs on the physical design parameters in MRRs. Leveraging these detailed models, we explore the design space of MRRs under FPVs to optimize the physical design parameters in these devices with a goal of enhancing their tolerance to FPVs while also improving their insertion loss and Q-factor. Simulation results obtained using an accurate finite difference eigenmode (FDE) solver [14] indicate the efficiency of our design optimization solution. Moreover, our study includes the design and fabrication of multiple MRRs using our novel design optimization solution. Experimental results from measuring several fabricated MRRs demonstrate a good agreement with our simulation results: on average, we indicate 70% reduction in the resonant wavelength shift in our fabricated MRRs. Note that thermal variations also impact MRR performance, but this work only focuses on FPVs.

The rest of the paper is organized as follows. Section II develops fundamental models to study the impact of FPVs on MRR performance. We present a comprehensive design space exploration for MRRs under FPVs in Section III. Leveraging such design space exploration, Section IV presents our design optimization solution for MRRs under FPVs, and includes fabrication results to validate this solution. Finally, we discuss our conclusions in Section V.

II. SILICON PHOTONIC MICRORING RESONATORS

Passive MRRs are the primary devices for wavelength-selective switching and multiplexing as well as optical filtering in PICs [5]. Fig. 1(a) indicates an MRR-based add-drop filter in which an MRR with a radius of R is in proximity with two parallel waveguides. Considering the coupling region in Fig. 1(a) (circled), the input/drop waveguide with a width and thickness of, respectively, w_w and t is in proximity with a gap of g to the MRR waveguide whose width and thickness are w_r and t, respectively (see Fig. 1(c)). Note that t is determined by the wafer SOI thickness and cannot be changed during design time. In contrast, both w_w and w_r can be determined during design time and they are often equal (i.e., $w_w = w_r$) in a conventional MRR-based add-drop filter design. Note that we assume the input and drop waveguides are identical.

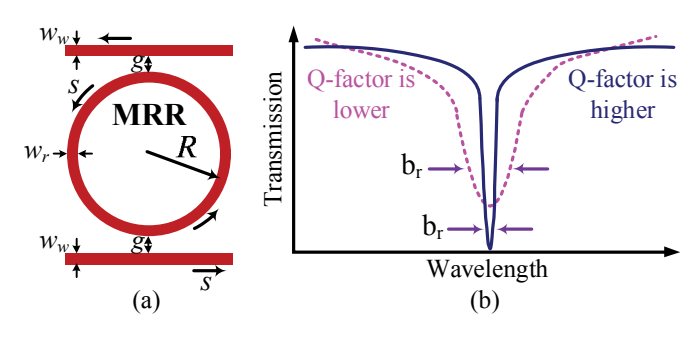


Fig. 2. (a) Cross-over (κ) and straight-through (s) coupling coefficients in an MRR with a radius of R and a gap of g; and, (b) An MRR through port response example to show a high quality factor (solid line) and a low quality factor (dotted line) in MRRs. Here, b_r is the bandwidth that is inversely proportional to Q-factor in MRRs: higher Q-factor results in lower bandwidth.

Considering an MRR with a resonant wavelength of λ_{MRR} and an input optical signal on a wavelength λ , the input signal couples and drops towards the drop port when $\lambda = \lambda_{MRR}$ (see Fig. 1(a)), whereas it passes the MRR towards the through port when $\lambda \neq \lambda_{MRR}$ [15]. This results in a Lorentzian-shape optical spectrum (see Fig. 1(b)). The resonant wavelength λ_{MRR} is a function of the critical dimensions of the MRR, including t, w_w, w_r , and R, in which any slight variations will deviate the resonant wavelength. Such deviation is known as the resonant wavelength shift $(\Delta \lambda_{MRR})$ (see Fig. 1(b)). The resonant wavelength λ_{MRR} can be modeled as:

$$\lambda_{MRR}(\lambda, w_{w/r}, t) = \frac{\pi R}{m} \left(n_{ew}(\lambda, w_w, t) + n_{er}(\lambda, w_r, t) \right), \tag{1}$$

where n_{ew} and n_{er} are, respectively, the effective indices of the optical mode in the input/drop waveguide and MRR waveguide, and m is an integer that denotes the order of the resonant mode. Note that n_{ew} and n_{er} can be calculated based on the propagation constant in waveguides and using various numerical methods [7]. Assuming the width (ρ_w) and thickness (ρ_t) variations on the input/drop waveguide and the MRR waveguide to be the same, the resonant wavelength shift $(\Delta \lambda_{MRR})$ in an MRR can be modeled based on the first order approximation of the waveguide dispersion [15] and (1):

$$\Delta\lambda_{MRR}(\lambda, w'_{w/r}, t') = \frac{2\lambda_{MRR}}{n_{gw} + n_{gr}} \left(\delta n_{ew/er} + \frac{n_{ew/er}}{R} \delta R \right). \tag{2}$$

Here, $w'_{w/r} = w_{w/r} \pm \rho_w$ and $t' = t \pm \rho_t$. Also, $\delta n_{ew/er}$ denotes the effective index changes due to the variations in waveguide width and thickness, while δR includes the variations in the MRR radius. In this paper, we assume $\delta R = 0$ to focus on the impact of waveguide width and thickness variations. Moreover, n_{gw} and n_{gr} are, respectively, the group indices of the optical mode in the input/drop waveguide and the MRR waveguide at the wavelength λ_{MRR} ($\lambda = \lambda_{MRR}$) that can be calculated as:

$$n_g(\lambda, w_{w/r}, t) = n_{ew/er} - \lambda \frac{dn_{ew/er}}{d\lambda}.$$
 (3)

FPVs also impact the power efficiency in MRRs, introducing extra losses when an optical signal passes or drops into an MRR. The insertion (or drop) loss (L, see (4)) is inversely

proportional to the coupling strength between the input/drop waveguide and the MRR waveguide [15], based on which we can study the impact of FPVs on the insertion loss in MRRs. Considering Fig. 2(a), we define κ as the cross-over coupling coefficient between the input waveguide and the MRR and s as the straight-through coefficient associated with the power that remains on the input waveguide. We assume a lossless coupler in which $|\kappa|^2 + |s|^2 = 1$. Both κ and s can be calculated precisely based on a recent method developed in [5]. Here, we develop a compact systematic model to indicate the impact of FPVs on the cross-over coupling coefficient κ in MRRs:

$$L^{-1} \propto \kappa(\lambda, w'_{w/r}, t') = f\left(n_{ew/er}(\lambda, w'_{w/r}, t'), g^{-1}, R\right),$$
(4)

in which f() is a function that can be defined based on the method described in [5]. Based on (4), κ is proportional to the effective indices of the optical mode in the input/drop and the MRR waveguide that change under FPVs. Moreover, it is directly proportional to the MRR radius (R) and inversely proportional to the gap (g): i.e., a larger gap (radius) will result in a lower (higher) coupling. Here, g is defined as the edge-to-edge gap between the input/drop waveguide and the MRR waveguide. Note that $w'_{w/r}$ and t' are defined for (2).

The quality factor (Q-factor) in an MRR is another parameter that will be affected under FPVs. Q-factor is a measure of the sharpness of the resonance relative to its central frequency that impacts the optical channel spacing, crosstalk, bandwidth, and many other characteristics in MRRs (see Fig. 2(b)). In particular, it is highly desirable to have MRRs with a high Q-factor in dense wavelength division multiplexing (DWDM) applications. Assuming a lossless coupler and employing (3) and (4), the Q-factor in an MRR-based add-drop filter under FPVs can be modeled as [15]:

$$Q(\lambda_{MRR}, w'_{w/r}, t') = \frac{\pi^2 R \sqrt{1 - \kappa^2} (n_{gw} + n_{gr})}{\lambda_{MRR} \kappa^2}.$$
 (5)

The developed analytical models in this section enable a comprehensive design space exploration of MRRs while considering the impact of variations in the waveguide width and thickness on the resonant wavelength, insertion loss, and Q-factor in MRRs. In particular, such models consider w_w and w_r as two separate input parameters, hence enabling analysis of MRRs in which w_w and w_r are equal or different: an important contribution of this paper. In the following sections, we show how such a feature along with our design space exploration contribute to optimizing the design parameters in MRRs to achieve higher tolerance to FPVs while also improving insertion loss and Q-factor in such devices.

III. MRR DESIGN SPACE EXPLORATION UNDER FABRICATION PROCESS VARIATIONS

The design space of MRRs can be divided into physical-level parameters (i.e., w_w , w_r and t) as well as device-level parameters (i.e., R and g). FPVs affect all of these parameters, but here we focus on the impact of physical-level parameters on MRR performance under FPVs. Among physical-level

parameters, only w_w and w_r can be determined during design time as t is limited by the SOI thickness on the host wafer (see Fig. 1(c)). In this section, an effort is made to study the impact of w_w and w_r on the tolerance of MRRs to FPVs. Here, we consider two case studies where $w_w = w_r$ and $w_w \neq w_r$.

Based on (2), one can redefine the total resonant wavelength shift $(T\Delta\lambda_{MRR})$ in an MRR by separating the contribution of width variations and that of thickness variations to the resonant wavelength shift in the MRR. Therefore, we have:

$$\begin{split} T\Delta\lambda_{MRR}(\lambda,w_{w/r}',t',\sigma_{w/t}) &= \\ \frac{\delta\lambda_{MRR}}{\delta w_{w/r}} \left(\frac{\sigma_{w_w} + \sigma_{w_r}}{2}\right) + \frac{\delta\lambda_{MRR}}{\delta t} \left(\frac{\sigma_{t_w} + \sigma_{t_r}}{2}\right). \end{split} \tag{6}$$

Here, $\frac{\delta \lambda_{MRR}}{\delta w_{w/r}}$ and $\frac{\delta \lambda_{MRR}}{\delta t}$ denote how much resonant wavelength shifts with respect to variations in the waveguide width and thickness, respectively (i.e., the resonant wavelength shift slopes). Moreover, σ_{w_w} and σ_{t_w} (σ_{w_r} and σ_{t_r}) are the standard deviations associated with the input/drop waveguide (MRR waveguide) width and thickness variations, respectively. Without loss of generality, we can safely assume $\sigma_w = \sigma_{w_w} = \sigma_{w_r}$ and $\sigma_t = \sigma_{t_w} = \sigma_{t_r}$: variations are the same on the input/drop and the MRR waveguide as they are in proximity [16]. Moreover, $\sigma_{w/t}$ can be quantified through various fabrications or obtained from a fabrication vendor.

The resonant wavelength shift slopes $(\frac{\delta \lambda_{MRR}}{\delta w_{w/r}})$ and $\frac{\delta \lambda_{MRR}}{\delta t}$ in (6) can be approximated using a linear model as the resonant wavelength in MRRs changes almost linearly with the variations in the waveguide width and thickness [16]. For instance, employing (2), $\frac{\delta \lambda_{MRR}}{\delta w_{w/r}}$ can be approximated as:

$$\frac{\delta \lambda_{MRR}}{\delta w_{w/r}} = \frac{\delta \lambda_{MRR}}{\left| \frac{\Delta \lambda_{MRR}(\lambda, w_{w/r} + \epsilon, t) - \Delta \lambda_{MRR}(\lambda, w_{w/r} - \epsilon, t)}{4\epsilon} \right|}{\epsilon},$$
(7)

in which ϵ is an arbitrary integer denoting a slight change in the waveguide width. Similarly, $\frac{\delta \lambda_{MRR}}{\delta t}$ can also be approximated. The models developed in (6) and (7) help us understand if altering w_w and w_r can impact the MRR tolerance to FPVs.

A. MRR Performance Analysis when $w_w = w_r$

Employing (6), (7), and Lumerical MODE [14], which is a commercial eigenmode solver and simulator, we quantitatively simulate the resonant wavelength shift slopes $\frac{\delta \lambda_{MRR}}{\delta w_{w/r}}$ and $\frac{\delta \lambda_{MRR}}{\delta t}$ in Fig. 3(a) when $w_w = w_r$. Results are shown for the fundamental transverse electric (TE) mode when t=220 nm and $\lambda=1550$ nm. We equally increase the input/drop and MRR waveguide widths from 300 to 1500 nm: $w_w = w_r \in [300, 1500]$ nm on the x-axis. There are two important observations from Fig. 3(a): first, the impact of width and thickness variations on the resonant wavelength is different (i.e., $\frac{\delta \lambda_{MRR}}{\delta w_{w/r}} \neq \frac{\delta \lambda_{MRR}}{\delta t}$); and, second, as the waveguide width increases (i.e., with wider MRRs), the impact of width variations decreases while the impact of thickness variations remains high and dominant (i.e., $\frac{\delta \lambda_{MRR}}{\delta t} > \frac{\delta \lambda_{MRR}}{\delta w_{w/r}}$). The same conclusion was drawn by the authors of [11], [12].

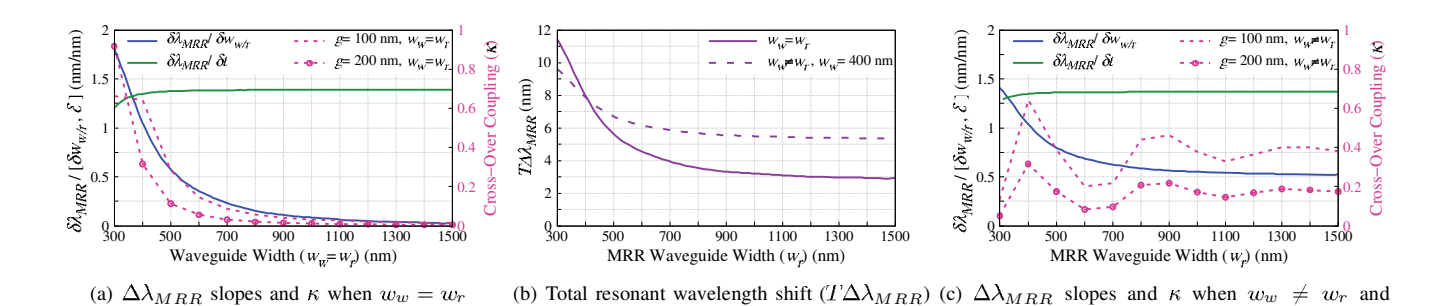


Fig. 3. (a) The resonant wavelength shift $(\Delta\lambda_{MRR})$ slopes and cross-over coupling coefficient (κ) in passive MRRs when $w_w=w_r$; (b) The total resonant wavelength shift $(T\Delta\lambda_{MRR})$ when $\sigma_w=5$ nm and $\sigma_t=2$ nm (see (6)); and, (c) The resonant wavelength shift slopes and cross-over coupling coefficient in passive MRRs when $w_w\neq w_r$. We consider t=220 nm and $\lambda=1550$ nm. Also, R=10 μ m when calculating κ in (a) and (c).

The fundamental mode confines better in the waveguide core as $w_w = w_r$ increases, hence width variations have less impact on the TE mode distribution in wider MRRs. Leveraging (6) and considering $\sigma_w = 5$ nm and $\sigma_t = 2$ nm (obtained from a SiPh foundry), Fig. 3(b) indicates the total resonant wavelength shift in passive MRRs, where $T\Delta\lambda_{MRR}$ decreases as $w_w = w_r$ increases (i.e., tolerance to FPVs increases).

In addition to the tolerance to FPVs, we consider insertion loss and Q-factor in passive MRRs. Studying the impact of increasing $w_w = w_r$ on the insertion loss in MRRs, we employ (4) to simulate the cross-over coupling (κ) in an MRR with $R=10~\mu \text{m}$ and q=100 and 200 nm, shown in Fig. 3(a). As can be seen, there is a critical issue when increasing $w_w =$ w_r in MRRs: although the tolerance to FPVs improves (see Fig. 3(b)), the cross-over coupling exponentially decreases as $w_w = w_r$ increases, substantially reducing the power dropped into MRRs, hence introducing severe insertion loss in MRRs. Moreover, considering (5) and Fig. 3(a), when κ decreases, the Q-factor increases exponentially to a point that the MRR will become impractical as its bandwidth will be very small (see Fig. 2(b)). In summary, our results demonstrate that increasing the waveguide width in passive MRRs when $w_w = w_r$ can improve the tolerance to FPVs, but at a cost of severe insertion loss and extremely low bandwidth (due to very high Q-factor) in such devices. This fact has been ignored in [11], [12] in which $w_w = w_r$. Towards addressing this issue, an effort is made to study passive MRR design space and performance (i.e., tolerance, insertion loss, and Q-factor) when $w_w \neq w_r$, which is another significant contribution of this paper.

B. MRR Performance Analysis when $w_w \neq w_r$

The cross-over coupling in MRRs is proportional to the overlap and the interaction between the optical modes in the input and the MRR waveguides. In principal, when increasing $w_w = w_r$ in an MRR, such an overlap will reduce as the fundamental optical mode will be more confined in the waveguide cores (i.e., farther from the waveguide edges), and hence κ decreases. To enhance κ in passive MRRs, we propose a solution based on considering $w_w \neq w_r$ and solely increasing w_r to possibly improve the tolerance to FPVs (i.e., $w_w < w_r$). To examine the effectiveness of this solution on various performance metrics in passive MRRs, using (6), (7),

and Lumerical MODE, we quantitatively simulate the resonant wavelength shift slopes when $w_w=400$ nm (considered as as example) and $w_r\in[300,1500]$ nm. As can be seen in Fig. 3(c), the impacts of width and thickness variations on the resonant wavelength of MRRs are similar to those indicated in Fig. 3(a). However, both $\frac{\delta \lambda_{MRR}}{\delta w_{w/r}}$ and $\frac{\delta \lambda_{MRR}}{\delta t}$ are slightly higher in Fig. 3(c) as $w_w < w_r$. Consequently, the total resonant wavelength shift when $w_w \neq w_r$ in Fig. 3(b) is also higher compared with that when $w_w = w_r$. Nevertheless, $T\Delta \lambda_{MRR}$ still decreases as w_r increases, indicating that our proposed solution can help improve the tolerance of passive MRRs to FPVs.

 $w_w = 400 \text{ nm}$

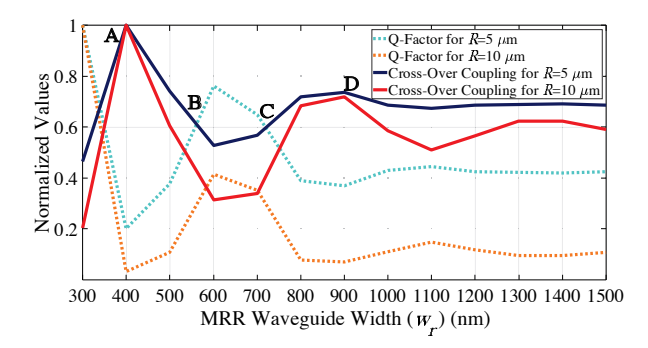
Fig. 3(c) shows the cross-over coupling performance when $w_w=400$ nm and $w_r\in[300,\ 1500]$ nm for an MRR with $R=10~\mu{\rm m}$ and g=100 and 200 nm. As can be seen, κ decreases at first as w_r increases, but it increases when $w_r\approx 2w_w$. We simulated κ with other values for w_w (not shown in the paper) and we found the same conclusion as the one in Fig. 3(c): κ increases when $w_r\approx 2w_w$. Furthermore, considering (5), $w_r\approx 2w_w$ can help improve the Q-factor in MRRs. This is an interesting finding as it shows that an optimal MRR design is feasible with high tolerance to FPVs, and acceptable cross-over coupling (compare κ in Figs. 3(a) and 3(c)) and Q-factor. Leveraging this finding, we study the optimal design space for passive MRRs in the next section.

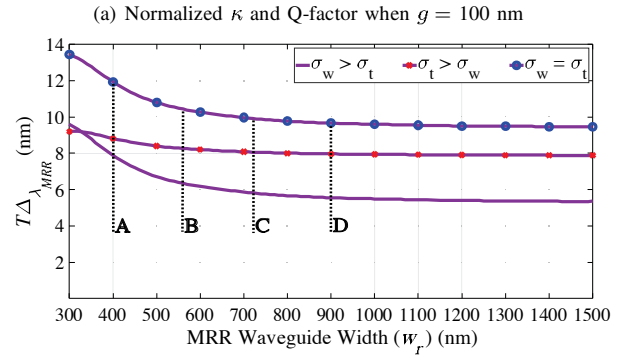
IV. MRR DESIGN OPTIMIZATION UNDER FABRICATION PROCESS VARIATIONS

This section presents a design optimization solution for MRRs under FPVs. We consider three performance metrics, including tolerance to FPVs, insertion loss (using the crossover coupling κ), and Q-factor. Considering Fig. 3, employing wider waveguides in MRRs can help improve their tolerance to FPVs. However, considering different performance metrics altogether, our design space exploration does not identify the values of w_w and w_r to achieve a high tolerance while also achieving a desirable κ and Q-factor in MRRs (κ and Q-factor are inversely proportional, see (5)). Therefore, given a $\sigma_{w/t}$ in (6), one can model the optimization problem as:

min
$$T\Delta\lambda_{MRR}(\lambda, w'_{w/r}, t', \sigma_{w/t})$$
 (8)
s.t. $\kappa \ge \kappa_m$ and $Q \ge Q_m$.

Here, κ_m and Q_m are, respectively, the minimum cross-over coupling and Q-factor that can be determined by the designer.





(b) Total resonant wavelength shift $(T\Delta \lambda_{MRR})$

Fig. 4. (a) Cross-over coupling (κ) and Q-factor calculated and normalized separately for two passive MRRs of $R=5~\mu{\rm m}$ and $R=10~\mu{\rm m}$ with $g=100~{\rm nm}$; and, (b) The total resonant wavelength shift for different values of σ_w and σ_t . Here, $w_w=400~{\rm nm}$ and $t=220~{\rm nm}$.

It is worth mentioning that, as discussed in Section III, device-level parameters (i.e., R and g) also impact the performance metrics considered in (8). However, our focus is on physical-level parameters (i.e., w_w and w_r) in this paper: finding the optimal values for w_w and w_r under different $\sigma_{w/t}$ that can satisfy the conditions in (8). As we will see, there are no single optimal values for w_w and w_r .

We address the optimization problem in (8) using an example described below. As a case study, we consider a passive MRR design with $R=5~\mu\mathrm{m}$ and $g=100~\mathrm{nm}$. Considering t = 220 nm, (8), and based on our finding in Section III-B (i.e., for $w_w < w_r$), we consider a fixed width of $w_w = 400$ nm on the input/drop waveguide while sweeping the width on the MRR waveguide from 300 to 1500 nm (x-axis in Fig. 4). Employing (4) and (5), Fig. 4(a) indicates the normalized cross-over coupling and Q-factor in the MRR when $w_r > w_w = 400$ nm. Taking into account different possible FPVs, we consider three scenarios where $\sigma_w = 5 \text{ nm} > \sigma_t = 2 \text{ nm}, \ \sigma_t = 5 \text{ nm} > \sigma_w = 2 \text{ nm},$ and $\sigma_w = \sigma_t = 2$ nm, based on which the total resonant wavelength shift is calculated and shown in Fig. 4(b). Note that the values assigned to $\sigma_{w/t}$ are obtained from a SiPh foundry and considered as an example. Considering Figs. 4(a) and 4(b) as well as the optimization problem in (8), a designer can determine w_r from different design points (DPs) specified in Fig. 4 (points A-D) based on various design preferences and different FPVs (here, $w_w = 400 \text{ nm}$):

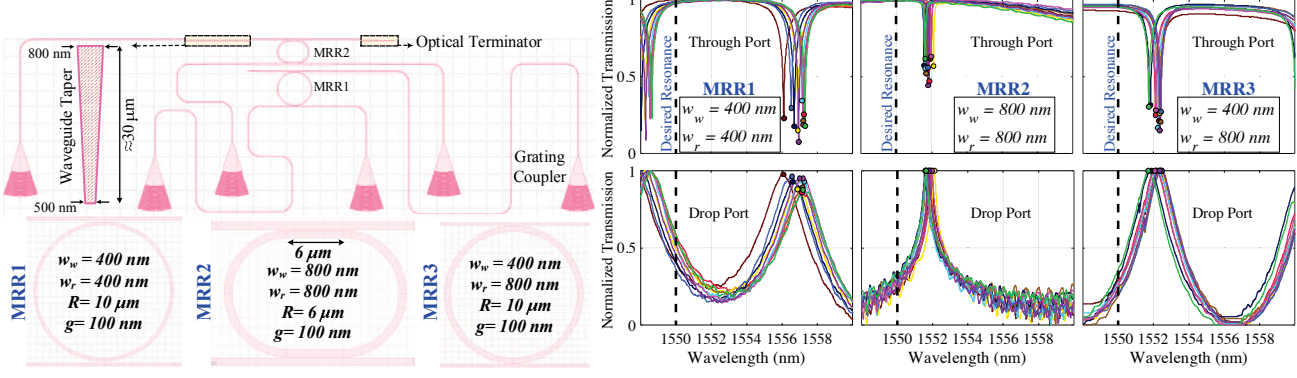
• κ -optimal (DP A, $w_r = 400$ nm): When high κ (i.e., low insertion loss) is desired. Consequently, the Q-factor

- is low at this point. Moreover, $T\Delta\lambda_{MRR}$ is high when $\sigma_w \geq \sigma_t$, necessitating increasing w_r for higher tolerance. Note that $T\Delta\lambda_{MRR}$ slightly improves when $\sigma_t > \sigma_w$. In summary, this is an optimal design point when low Q-factor is acceptable $(Q_m$ is small in (8)) and $\sigma_t >> \sigma_w$.
- Q-optimal (Design region between DPs B and C: 560 nm $< w_r < 720$ nm): When high Q-factor is desired. Consequently, κ is low in this region (\approx 40% lower than DP A). Also, $T\Delta\lambda_{MRR}$ slightly improves when $\sigma_t > \sigma_w$. In summary, this is an optimal design space when low κ is acceptable (κ_m is small in (8)) and $\sigma_t > \sigma_w$.
- Design region between DPs C and D (720 nm $\leq w_r \leq$ 900 nm): Q-factor and κ are not as worse as those at DP A and the design region between DPs B and C, respectively. Therefore, a trade-off can be made to design an MRR with a relatively high κ and high Q-factor. Most importantly, considering Fig. 4(b), $T\Delta\lambda_{MRR}$ slightly improves among all different values of σ_w and σ_t as w_r increases, hence tolerance is also high under different FPVs in this design region.

It is worth mentioning that our proposed design optimization solution is not specific to the aforementioned MRR example and $w_w = 400$ nm consideration, hence it is applicable to any MRR design problem. For instance, Fig. 4(a) indicates the results for another MRR with $R = 10 \mu m$ and q = 100 nm. As can be seen, similar design regions can be defined, while DPs are slightly different. Moreover, one may question maintaining a single-mode operation when increasing waveguide widths as higher-order modes exist in wide waveguides ($w_{w/r} > 500 \text{ nm}$ when t = 220 nm) [6]. While multimode waveguides are useful for mode-division multiplexing, single-mode operation can be obtained in our solution based on adiabatically increasing MRR waveguide width [13], or by using waveguide tapers [11]. Our proposed optimization solution is a significant step towards designing high-performance MRRs under random FPVs. In the next section, we apply this optimization solution to the design and fabrication of multiple MRRs to experimentally verify the efficiency of our proposed solution.

A. Fabrication Results

We designed three passive TE-polarized MRR-based adddrop filters with g = 100 nm to experimentally validate our proposed optimization solution. Considering Fig. 5(a), these include MRR1 based on DP A in Fig. 4 ($w_w = w_r = 400 \text{ nm}$), MRR2 using the solution in [11] ($w_w = w_r = 800$ nm), and finally MRR3 based on the design region specified by DPs C and D in Fig. 4 ($w_w = 400$ nm and $w_r = 800$ nm). Also, $R = 10 \mu \text{m}$ in MRR1 and MRR3. Note that for MRR2, a racetrack resonator is considered with $R=6~\mu\mathrm{m}$ and a coupler length of 6 μm to ensure enough coupling (see κ in Fig. 3(a)). Ten identical copies of each MRR (30 MRRs in total) were placed on a 1.5×0.6 mm² chip fabricated by a high-resolution electron beam (EBeam) lithography system. Fig. 5(a) indicates an example of a unit cell of the designed MRRs with grating couplers designed for 1550 nm quasi-TE operation. Moreover, waveguide tapers with lengths of



(a) A unit cell example (top) and details of fabricated MRRs (bottom)

(b) Measurement results (30 MRRs)

Fig. 5. (a) An example of the cell layout (top, MRR1 and MRR2 only) of the fabricated MRRs with their specifications (bottom); and, (b) Measured through and drop port responses obtained by testing 30 identical copies of MRRs in (a). All the MRRs were designed to resonate at 1550 nm (desired resonance).

 \approx 10 and 30 μ m (see Fig. 5(a)) are employed to ensure a single-mode operation. Furthermore, 220 nm thick SOI strip waveguides with a 500 nm width are used for routing.

Using an automated testing facility with no thermal variations, Fig. 5(b) indicates the measured through and drop port responses of 30 identical copies of MRRs indicated in Fig. 5(a). Resonant peaks that are specified by circles all belong to the same resonant mode. Moreover, all the MRRs were designed to resonate at 1550 nm (desired resonance in Fig. 5(b)). As can be seen, there is an excellent agreement between our simulation results in Fig. 3 and design optimization solution explored in Fig. 4 with fabrication results in Fig. 5(b). From Figs. 4 and 5(b), it can be seen that MRR1 has the best κ and the worst Q-factor with an average total resonant wavelength shift of 7.1 nm among the ten resonant peaks. The average total resonant wavelength shift in MRR2 is reduced to 1.8 nm, but κ is too low, hence there is noise on the drop port (Fig. 5(b)), making the Q-factor extremely high and impractical due to the extremely narrow bandwidth. Finally, MRR3 (designed based on our proposed optimization solution) indicates an average total resonant wavelength shift of 2.1 nm, and an acceptable κ and Q-factor. Note that although we did not experimentally measure κ and Q-factor in MRR1–3, the through and drop port responses in Fig. 5(b) clearly support the aforementioned comparisons among the MRRs. Another important observation from Fig. 5(b) is that the resonant peaks are more uniform in MRR3, whereas they are more spread-out in MRR1, simplifying the tuning circuit design for MRR3.

V. CONCLUSION

For the first time, this paper presents a comprehensive design space exploration of the physical parameters of microring resonators under fabrication process variations. In particular, we develop analytical models required to study the resonant wavelength shift, cross-over coupling, and quality factor in MRRs under variations. Leveraging these comprehensive models, a design optimization solution is developed to find optimal physical design parameters in MRRs, enhancing their tolerance to fabrication process variations while improving insertion loss (through coupling) and Q-factor in such devices.

Furthermore, we experimentally validate the efficiency of our proposed design optimization solution through fabricating and measuring multiple MRRs. Our study indicates the importance of design space exploration in silicon photonic devices that can lead to a meaningful design optimization. This is an excellent example of applying design concepts in electronic design automation (EDA) to silicon photonics design, where our proposed design optimization solution can be easily integrated into an MRR design automation tool.

REFERENCES

- [1] Y. Shen et al., "Silicon photonics for extreme scale systems," IEEE/OSA J. Lightw. Technol., vol. 37, no. 2, pp. 245–259, 2019.
- [2] Z. Zhou et al., "Development trends in silicon photonics for data centers," *Optical Fiber Technology*, vol. 44, pp. 13–23, 2018.
- [3] Y. Shen et al., "Deep learning with coherent nanophotonic circuits," Nat. Photonics, vol. 11, no. 7, pp. 441–446, 2017.
- [4] T. Y. L. Ang et al., "How small can a microring resonator be and yet be polarization independent?" Appl. Opt., vol. 48, no. 15, pp. 2821–2835, 2009
- [5] M. Bahadori et al., "Design space exploration of microring resonators in silicon photonic interconnects: Impact of the ring curvature," IEEE/OSA J. Lightw. Technol., vol. 36, no. 13, pp. 2767–2782, 2018.
- [6] L. Chrostowski et al., "Impact of fabrication non-uniformity on chipscale silicon photonic integrated circuits," in OFC, 2014, p. Th2A.37.
- [7] M. Nikdast et al., "Chip-scale silicon photonic interconnects: A formal study on fabrication non-uniformity," *IEEE/OSA J. Lightw. Technol.*, vol. 34, no. 16, pp. 3682–3695, 2016.
- [8] W. A. Zortman et al., "Silicon photonics manufacturing," Opt. Express, vol. 18, no. 23, pp. 23 598–23 607, 2010.
- [9] M. Bahadori et al., "Thermal rectification of integrated microheaters for microring resonators in silicon photonics platform," *IEEE/OSA J. Lightw. Technol.*, vol. 36, no. 3, pp. 773–788, 2018.
- [10] C. Sun et al., "A 45nm SOI monolithic photonics chip-to-chip link with bit-statistics-based resonant microring thermal tuning," in *IEEE VLSI Circuits*, 2015.
- [11] M. Nikdast et al., "DeEPeR: Enhancing performance and reliability in chip-scale optical interconnection networks," in GLSVLSI, 2018.
- [12] Y. Luo et al., "A process-tolerant ring modulator based on multi-mode waveguides," *IEEE Photon. Technol. Lett.*, vol. 28, no. 13, pp. 1391– 1394, 2016.
- [13] Z. Su et al., "Reduced wafer-scale frequency variation in adiabatic microring resonators," in OFC, 2014, p. Th2A.55.
- [14] Lumerical Solutions Inc. Lumerical MODE. [Online]. Available: http://www.lumerical.com/tcad-products/mode/
- [15] W. Bogaerts et al., "Silicon microring resonators," Laser & Photonics Reviews, vol. 6, no. 1, 2012.
- [16] Z. Lu et al., "Performance prediction for silicon photonics integrated circuits with layout-dependent correlated manufacturing variability," Opt. Express, vol. 25, no. 9, pp. 9712–9733, 2017.